Structure, Dielectric Properties and Impedance Spectroscopy of $BaTi_{0.97}(Zn,V,Ta)_{0.03}O_3$ Ceramics

[1]Raz Muhammad*, [2]Sajid Ali, [2]Yaseen Iqbal, [1]Amir Khesro and [2]Muhammad Uzair
[1]*Department of Physics, Abdul Wali Khan University Mardan, Garden Campus 23200 Mardan, KP, Pakistan.*
[2]*Materials Research Laboratory, Department of Physics, University of Peshawar, 25120 Peshawar, KP, Pakistan.*
raz@awkum.edu.pk*

(Received on 18th December 2018, accepted in revised form 3rd May 2019)

Summary: $BaTi_{0.97}Zn_{0.01}V_{0.01}Ta_{0.01}O_3$ sample was prepared using the conventional mixed oxide sintering route. The samples were characterized using X-ray diffraction, Raman spectroscopy, Scanning Electron Microscopy and Impedance spectroscopy. Structure of the sample was analyzed using Rietveld analysis which showed the formation of tetragonal symmetry. Raman spectroscopy was also in agreement with the XRD results, further indicating the ferroelectric signature in the sample. Electrical microstructure analyzed by impedance spectroscopy analysis revealed two electroactive regions in the sample, belonging to the grain boundary and bulk. An extrinsic conduction mechanism was observed across the sample. Dielectric properties as a function of temperature demonstrated phase transition (T_C) at ~ 94 °C, with relative permittivity ~ 3280 at T_C. Antiferroelectric-like double hysteresis loops were observed in P-E analysis. The energy storage density was calculated to be 0.26 J/cm^3 at an electric field of 50 kV/cm, indicating that $BaTi_{0.97}Zn_{0.01}V_{0.01}Ta_{0.01}O_3$ ceramics can be potentially useful base materials for high density energy storage capacitors.

Keywords: $BaTiO_3$; Ferroelectrics; Dielectric properties; Impedance spectroscopy, Ceramics.

Introduction

The importance of a dielectric material can be determined primarily by its relative permittivity, temperature stability, and breakdown strength for use in capacitors and high energy density storage applications. $BaTiO_3$ (BT) is an important perovskite structured material. BT-based ceramics are mostly used in MLCC (multi-layer ceramic capacitors), PTCR (positive temperature coefficient resistors) and thermistors [1, 2]. At Curie temperature (T_C), relative permittivity (ε_r) of BT is ~ 10000 [3] that varies with grain size [4]. The optimum sintering temperature (ST) of BT ranges from 1350-1400ºC and different methods are used to lower ST of BT based ceramics [5-8]. It is technologically as well as commercially important to lower ST to cut down the processing costs and to lower it than the melting point of electrode such as Ni and Cu in MLCCs. Ceramic capacitor can store electric energy with much higher power output than the conventional batteries. However, their poor storage capacity compared to batteries is a challenge for researchers. Anti-ferroelectric materials have far higher power density than ferroelectrics. So far, lead based materials have shown excellent properties because of their anti-ferroelectric characters. Lead free ceramics are preferred because of the toxic nature of lead (Pb) and BT-based materials are one of the choices because of its high ε_r. The co-doping of Ta_2O_5 and ZnO in BT has been reported to increase T_c and ε_r along with a decrease in sintering temperature [9]. The melting point of Zn and V is low which may be useful to decrease the sintering temperature in comparison to pure BT. In this study, Zn, Ta and V were substituted for Ti in BT according to the formula $BaTi_{0.97}Zn_{0.01},V_{0.01}Ta_{0.01}O_3$ and the resulting ceramics and their structure and electrical properties were studied.

Experimental

$BaTi_{0.97}Zn_{0.01}V_{0.01}Ta_{0.01}O_3$ samples were prepared using reagent grade $BaCO_3$, TiO_2, ZnO, V_2O_5 and Ta_2O_5 (Sigma Aldrich) through solid state sintering route. All reagents were dried at appropriate temperatures to get rid of the adsorbed moisture. The dried reagents were batched according to the molar ratios of the composition and then ball milled for 12 h. After ball milling, the powders were calcined at 950 °C for 6 h at a ramp rate of 5 °C/min. The calcined powders were re-milled again to reduce particle size and get rid of any agglomerates. The resulting free flowing powders were pressed into green pellets using a uniaxial pellet presser at ~50 MPa. The green pellets were densified into compact ceramics by sintering at 1100-1250 °C for 4 h at a heating/cooling rate of 5 °C/min.

*To whom all correspondence should be addressed.

The density of sintered samples was measured using a high precision densitometer (MDs-300). Phase of the sintered samples was identified using Siemens X-ray diffractometer with Cu-Kα radiation source. Rietveld analysis of the sample was carried out using GSAS+EXPGUI computer program [10]. Raman spectra of the samples were obtained using a Renishaw Raman spectrometer (New Mills, Wotton-Under-Eagle, UK). Polarization vs electric field (P-E) loops were obtained using a ferroelectric test system. A JSM-5910 (JEOL) SEM (scanning electron microscope) was used for microstructural analysis. Temperature dependent ε_r and dielectric loss (tanδ) were studied in the temperature range ~ 20 to 250 °C using an Agilent LCR meter (HP 4284A). Complex Impedance spectroscopy (CIS) of the samples was performed using an Agilent (E4980A) Impedance Analyzer in the temperature range 300-500 °C.

Results and Discussion

X-rays diffraction trace recorded for sintered $BaTi_{0.97}V_{0.01}Ta_{0.01}Zn_{0.01}O_3$ sample is shown in Fig. 1. The XRD peaks matched PDF # 74-1959 for tetragonal BT with space group *P4mm*. A low intensity additional peak (labeled as '*') was observed at ~ 27.6º which could not be identified. The intensity ratio of the observed (002) and (200) XRD peaks was 1:2 which further confirmed tetragonal symmetry for the sintered phase [11]. The strongest peak at 45.3º was selected and yielded the average crystallite size to be 35 nm. The structure was further confirmed using Rietveld analysis which converged for the tetragonal (*P4mm*) structure. The refined lattice parameters were a = b = 4.0003(2) Å and c = 4.0226(3) Å. The extracted refined parameters are listed in Table-1. Here, Ba^{2+} with larger ionic radius occupy A-site and intermediate size cations (Ti^{4+}, Ta^{5+}, Zn^{2+} and V^{5+}) occupy B-site of the host lattice. Oxygen (O1 and O3) ions are at the anionic site occupying 1*b* and 2*c* positions, respectively as shown in Fig. 2.

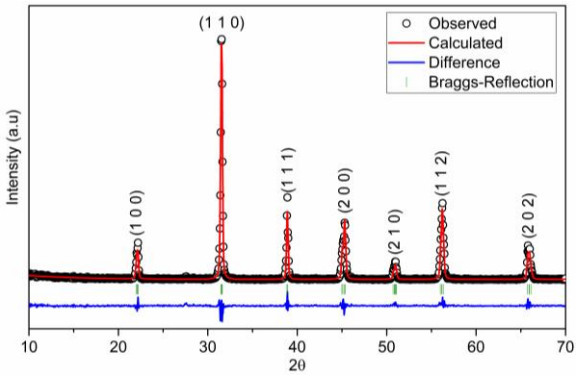

Fig. 1: Observed, calculated and difference in the XRD patterns of $BaTi_{0.97}(Zn,V,Ta)_{0.03}O_3$ sample sintered at 1200ºC for 4h.

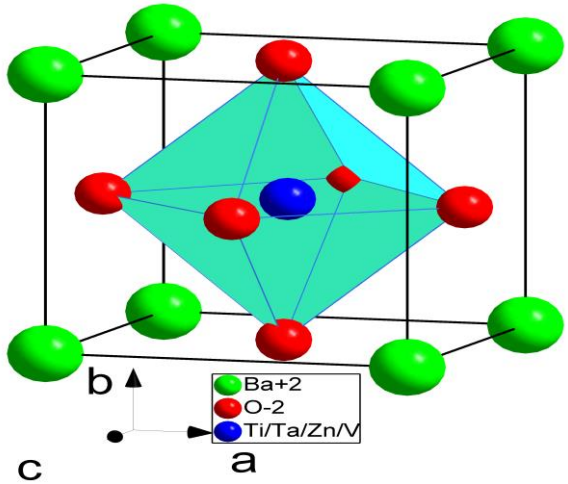

Fig. 2: Unit cell of $BaTi_{0.97}(Zn,V,Ta)_{0.03}O_3$.

Table-1: Structural data of $BaTi_{0.97}V_{0.01}Ta_{0.01}Zn_{0.01}O_3$ sample.

Crystal system	**Tetragonal**					
Space group	***P*4mm (no. 99)**					
Unit cell dimensions	***a* = 4.0003(2) Å**					
	***c* = 4.0226(3) Å**					
Cell volume	**64.37(0) Å^3**					
Z	**1**					
Density, calculated	**6.064 g/cm^3**					
R_P	**0.1454**					
R_{WP}	**0.2092**					
Goodness of fit (χ^2)	**1.45**					
Atomic coordinates and isotropic displacement parameters						
Atom	**Wyckoff Position**	**Occupancy**	**x**	**y**	**z**	**U**
Ba^{+2}	**1*a***	**1**	**0**	**0**	**0**	**0.0071**
Ti^{+4}	**1*b***	**0.97**	**1/2**	**1/2**	**0.48200**	**0.0112**
Ta^{+5}/V^{+5}/Zn^{+2}	**1*b***	**0.01**	**1/2**	**1/2**	**0.48200**	**0.0112**
O1 (O^{-2})	**1*b***	**1**	**1/2**	**1/2**	**-0.04582**	**0.0000**
O2 (O^{-2})	**2*c***	**1**	**1/2**	**0**	**0.51451**	**0.0000**

The crystallite size was determined using the full widths at half maximum (FWHM) employing the Debye–Scherrer equation (1)

$$\mathbf{d = \frac{k\lambda}{\beta\cos\theta}} \qquad (1)$$

where *d* is the crystallite size, and λ is the wavelength of Cu Kα-X-ray radiation (0.15405 nm), β is the full-width half maxima (FWHM) in radians and θ is the diffraction angle. The secondary electron SEM image of $BaTi_{0.97}V_{0.01}Ta_{0.01}Zn_{0.01}O_3$ sample sintered at 1200°C for 4h is shown in Fig. 3. The dimensions of the observed grains of almost uniform contrast varied from ~1 to 4 μm.

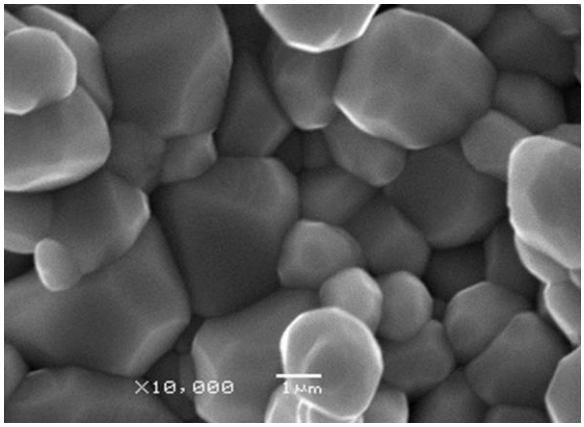

Fig. 3: SEM micrograph of $BaTi_{0.97}(Zn,V,Ta)_{0.03}O_3$ sample sintered at 1200ºC for 4h.

The Raman spectrum of $BaTi_{0.97}V_{0.01}Ta_{0.01}Zn_{0.01}O_3$ sample taken at room temperature (RT) is shown in Fig. 4. $BaTiO_3$ has five atoms and fifteen degrees of freedom per unit cell [12]. The 180 cm^{-1} mode is ascribed to interference of Raman scattering between two vibrational modes with overlapping frequency. The interference arises due to an an-harmonic band between the two layer vibrational modes [13]. Tetragonal BT phase is known to exhibit Raman scattering bands at ~250, 515 and 717 cm^{-1} and a sharp peak at ~306 cm^{-1}. Theoretically, the phase with cubic (*Pm*3*m*) symmetry exhibits no Raman active common modes but commonly exhibits broad bands at ~250 and 515 cm^{-1}, originating from the local-disorder coupled with the position of Ti^{4+} ions. The bands near 717 cm^{-1} in the tetragonal structure is due to Ba^{2+} defects in the BT lattice. A small mode appearing at ~838 cm^{-1} is due to the aliovalent substituents on the B-site in BT while such a mode does not appear due to substitutions on the A-site in BT [14]. This mode arises due to the charge difference at equivalent sites in BT. In conclusion, the Raman spectrum confirms that the V-, Ta- and Zn-doped composition crystallized into a tetragonal symmetry, consistent with the previous studies [15-17].

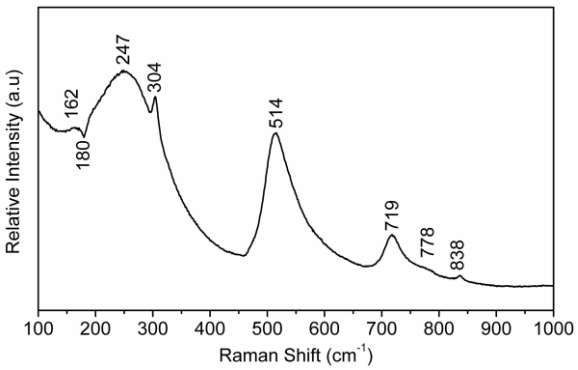

Fig. 4: Raman spectrum of $BaTi_{0.97}(Zn,V,Ta)_{0.03}O_3$ ceramics.

To analyze the electrical microstructure of the sample, impedance spectroscopy which is considered as a powerful tool to differentiate between different electroactive regions? The complex plane plots (Z'' versus Z') at 300 and 450ºC showed a large semicircle at low frequency and smaller semicircle at high frequency (Fig. 5) which indicated the presence of two different conduction mechanisms. The large semicircle observed at low frequency was indicative of a relatively more resistive region while the small semicircle observed at high frequency was indicative of a relatively more conductive region. The arc at high frequency is related to the bulk while the arc at low frequency originates from contributions due to the grain boundaries. The modulus plot also showed the same behavior, Fig. 6.

To further confirm, the combined spectroscopic plot (Z'' and M'' versus logf) was also analyzed, Fig. 7. Consistent with the complex plane plot (Fig. 5), two peaks were observed on the spectroscopic plot (Z'' versus logf) as well. The value of resistance (R) and capacitance (C) were obtained from the peak maxima in the spectroscopic plots using formula $R = 2Z''_{max}$ and $C = 1/(2\pi f_{max}R)$, respectively. At 450 °C, the capacitance and resistance values calculated from Z'' versus logf plot were 1.3×10^{-9} F and 1.5 MΩ, respectively. Similarly, the capacitance and resistance values obtained from the M'' versus logf plot were 27.2×10^{-12} F and 5841 Ω, respectively. The capacitance versus logf plot shown in Fig. 8 was found in good agreement with the capacitance values associated with the bulk (10^{-12} F) and grain boundary (10^{-9} F) [18, 19]. To study the conduction mechanism in the sample, activation energies were calculated from the Arrhenius plot of conductivity (Fig. 9), using equation (2)

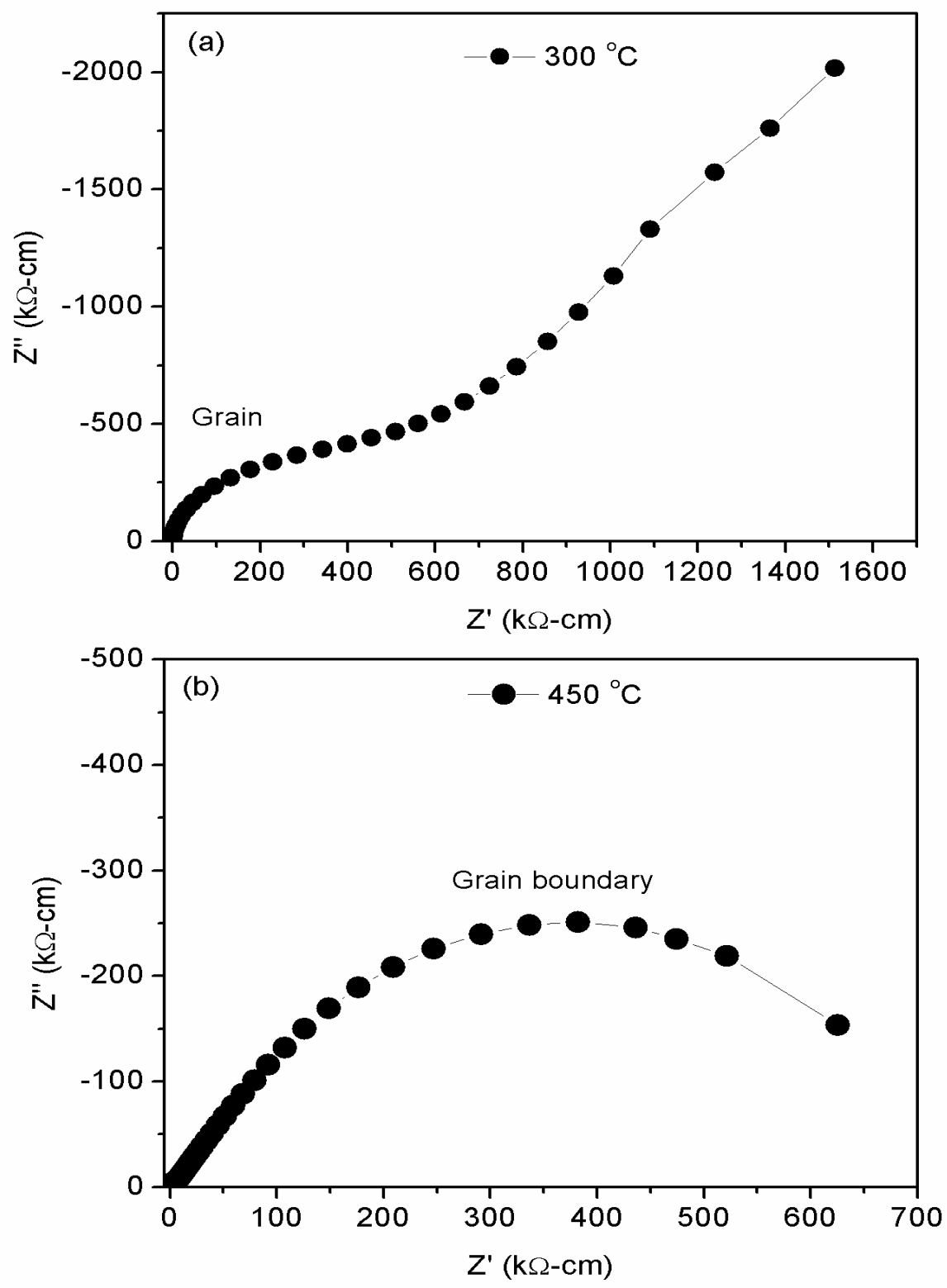

Fig. 5: Complex plane plots (Z' vs Z″) at a) 300ºC and b) 450ºC.

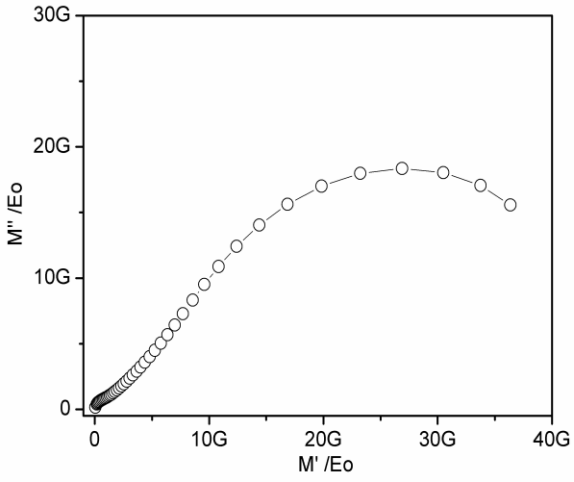

Fig. 6: Modulus plot (M' vs M″) at 450ºC.

$$\sigma = \sigma_{\circ} \exp\left(\frac{-E_a}{k_\beta T}\right) \quad (2)$$

where $\sigma_{\circ}$ is the pre-exponential factor, T is the temperature, E_a is activation energy and k_β is Boltzmann constant. E_a of the bulk and grain boundary were calculated to be 1.04 eV and 1.22 eV, respectively, which suggest that the extrinsic conduction (oxygen ion conduction) takes place in the samples which is commonly reported for pure BT.

ε_r and tanδ plots of $BaTi_{0.97}Zn_{0.01}V_{0.01}Ta_{0.01}O_3$ at 1 kHz to 1 MHz in the temperature range ~25-250 °C are shown in Fig. 10. ε_r at the peak temperature was observed to be ~ 3280. The phase transition temperature (Curie temperature T_C) of undoped BT is commonly reported to be ~ 125 °C; however, doping with V, Ta and Zn shifted the Curie temperature to a relatively lower temperature (~ 94 °C). The Curie temperature of BT basically depends on the domain structure, particle size and electrical behavior of the grain boundary [20-22] which makes the explanation of the phase transition behavior of BT difficult. Similarly, covalency also affects ε_r of BT which may be a possible reason for the observed decrease in T_C [20, 23]. tanδ was ~ 0.008 at room temperature.

The P-E loops of $BaTi_{0.97}Zn_{0.01}V_{0.01}Ta_{0.01}O_3$ sample were measured by exposing the samples to electric fields between 10 - 50 kV/cm as shown in Fig. 11. The sample exhibited antiferroelectric like behavior at all E values showing nearly zero polarization at room temperature, suggesting that the total energy can be released by removing electric field. The observed double hysteresis loop is typical of antiferroelectric components prototyped by $PbZrO_3$ [24]. It should be noted that double hysteresis can have other origins such as Paraelectric-Ferroelectric (PE-FE) phase transition near T_C and / or an aging effect well below T_C [25]. Since, the observation of double hysteresis loops in the present study were at room temperature (well below T_C); therefore, these could not be attributed to the PE-FE phase transition but are more likely to be arising of an effect similar to aging, as observed by Ren et al for aged Mn doped BT [26]. Generally double loops due to aging are attributed to gradual stabilization of domain patterns by defects such as vacancies, dopant and or impurities. Though these samples were not aged but the role of defects in pinching of the P-E loops cannot be excluded. Defects in the studied sample could be associated to presence of impurities such as Fe^{3+} in reagents and/or volatilization of V^{5+} during high temperature synthesis. The exact role of defects is not clear at this stage and warrants a systematic investigation, however regardless of the origin, double loops are favored for energy storage applications due to their low remnant polarization. Generally, KBT based ceramics have been extensively investigated for high energy density applications. More recently, Yu et al. reported 1.15 J/cm^3 under 105 kV/cm for BNT-BKT-BA system [27]. At E = 50 kV/cm, the energy storage density was 0.26 J/cm^3 for $BaTi_{0.97}Zn_{0.01}V_{0.01}Ta_{0.01}O_3$ sample which may be increased at higher E values, below breakdown of the sample. Therefore, further work is required to study the electric breakdown and hence maximum energy storage ability of $BaTi_{0.97}Zn_{0.01}V_{0.01}Ta_{0.01}O_3$ sample. The energy efficiency of the sample at 50 kV/cm was found to be 72 %. There are several lead-based antiferroelectric materials that are found to be excellent for high energy storage applications, but environmentally friendly materials are required for these applications. On the other hand, there are very few lead-free anti-ferroelectric materials therefore, $BaTi_{0.97}Zn_{0.01}V_{0.01}Ta_{0.01}O_3$ ceramics could be an ideal lead-free material for high energy storage applications. Furthermore, the sintering temperature of $BaTi_{0.97}Zn_{0.01}V_{0.01}Ta_{0.01}O_3$ ceramics is almost 150 °C lower than the BT prepared via conventional mixed oxide sintering route [3].

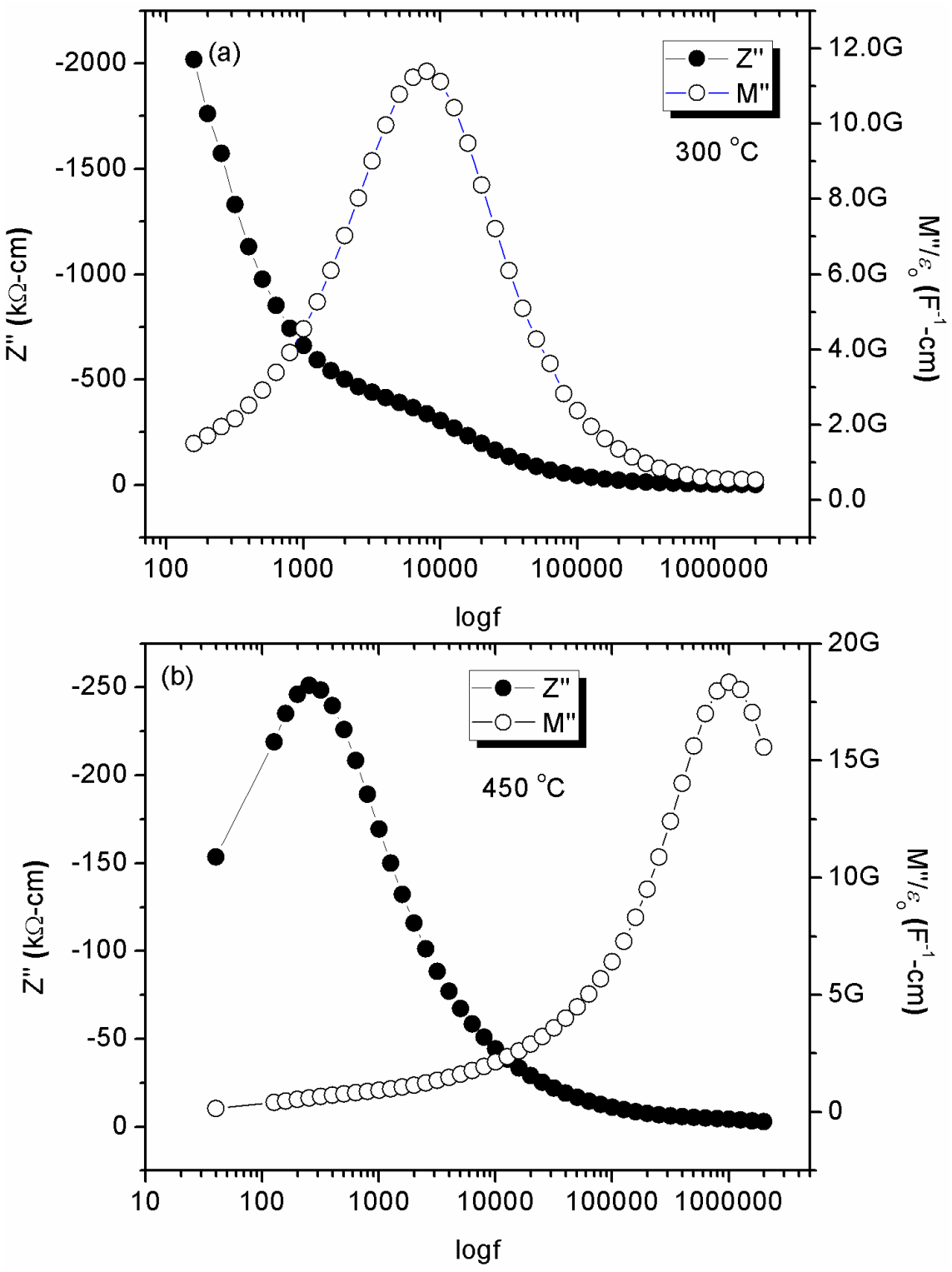

Fig. 7: Impedance spectroscopic plots of $BaTi_{0.97}(Zn,V,Ta)_{0.03}O_3$ ceramics at; a) 300ºC and b) 450ºC.

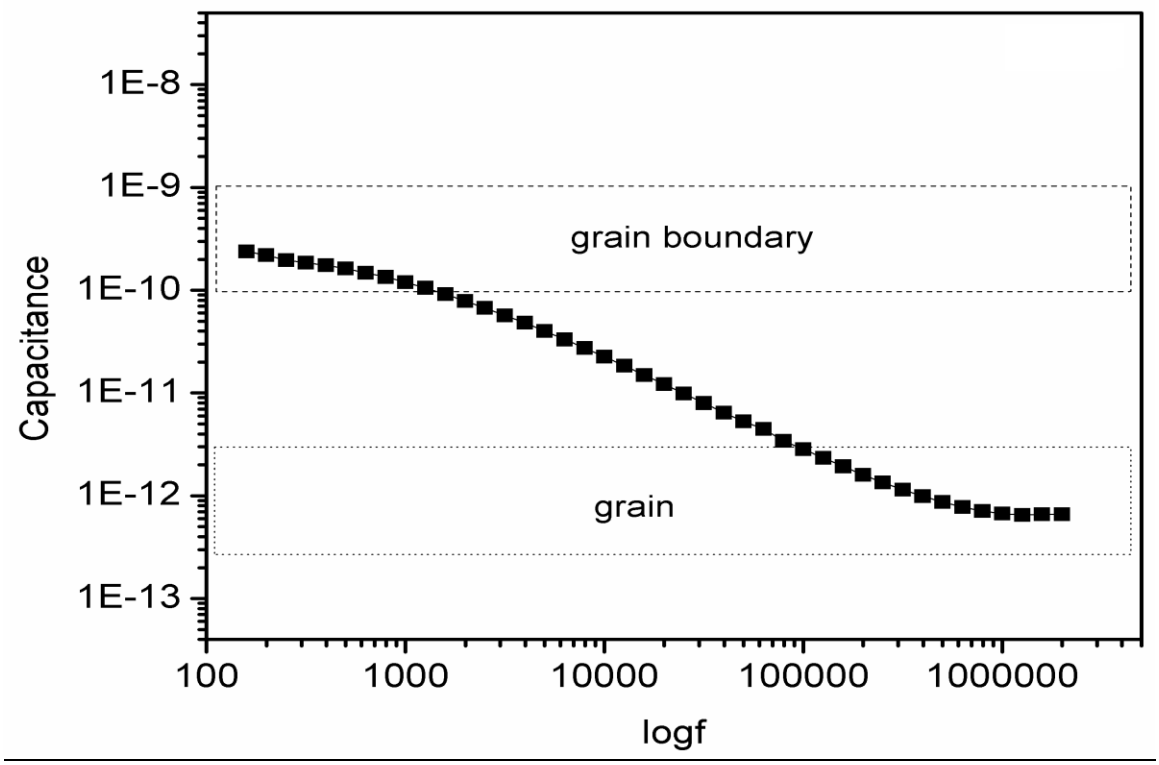

Fig. 8: Plot of logC vs. logf for $BaTi_{0.97}(Zn,V,Ta)_{0.03}O_3$ sample at 300ºC.

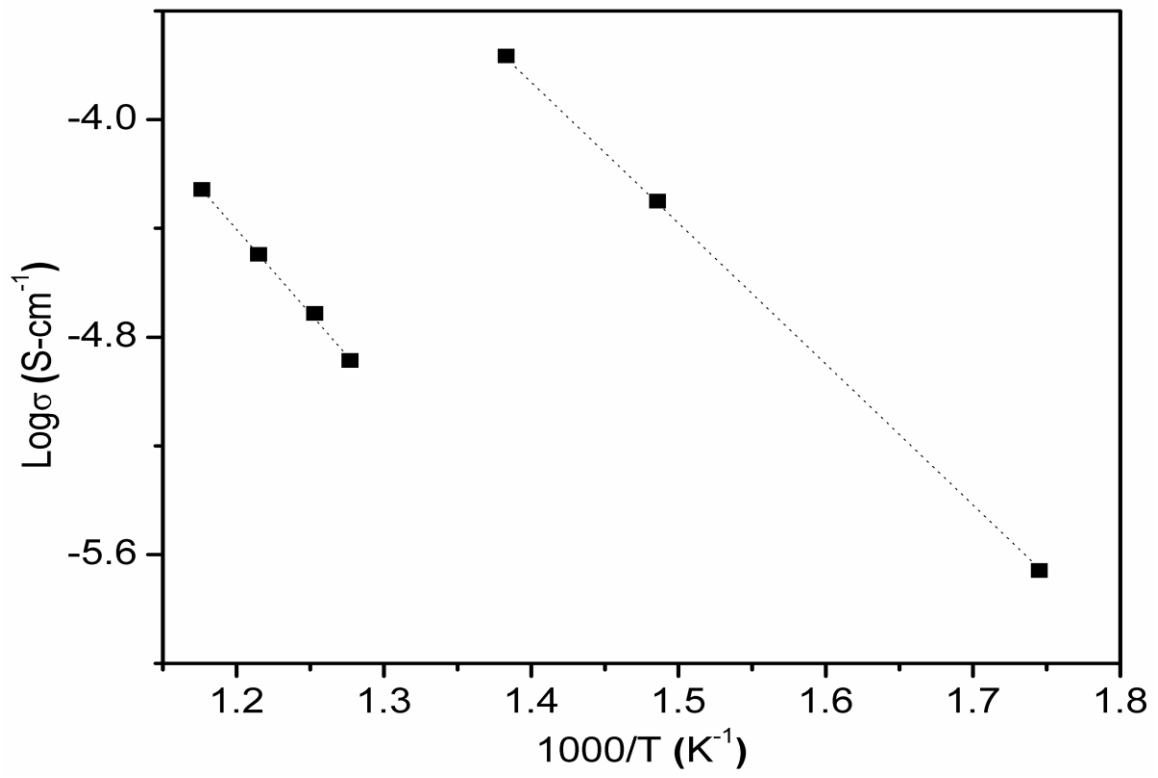

Fig. 9: Arrhenius plot of conductivity for $BaTi_{0.97}(Zn,V,Ta)_{0.03}O_3$ ceramics.

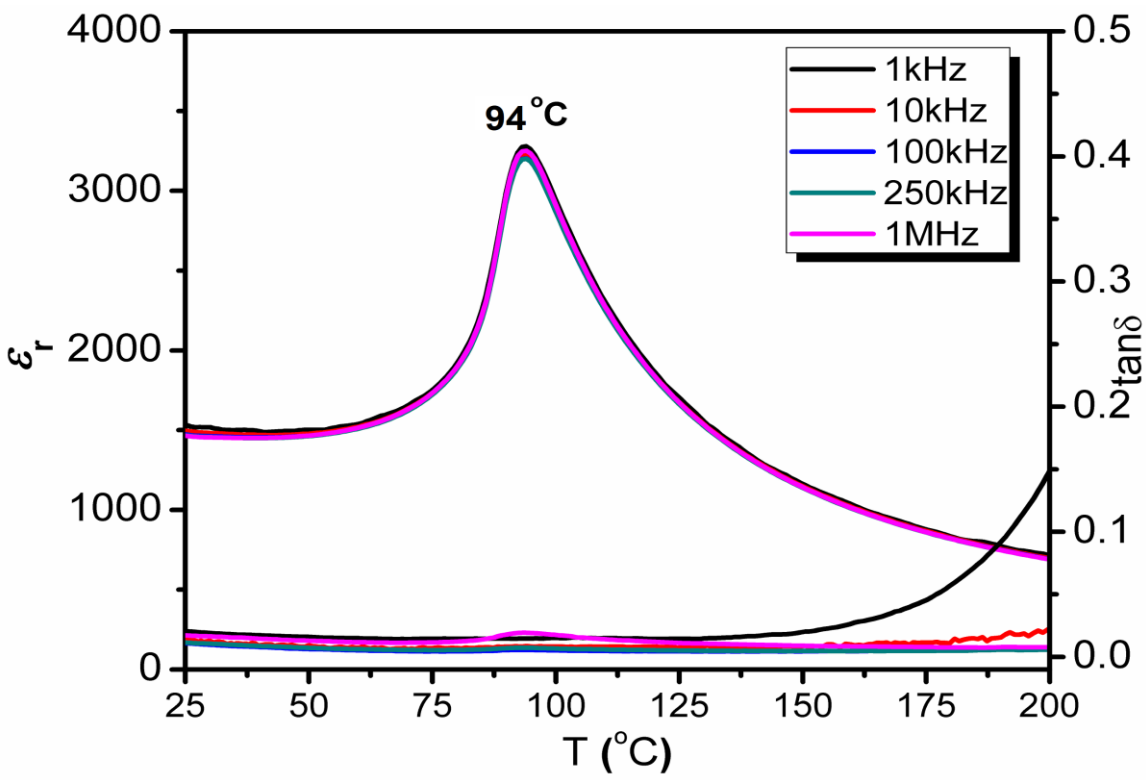

Fig. 10: ε_r and tanδ versus temperature for $BaTi_{0.97}(Zn,V,Ta)_{0.03}O_3$ at different frequencies.

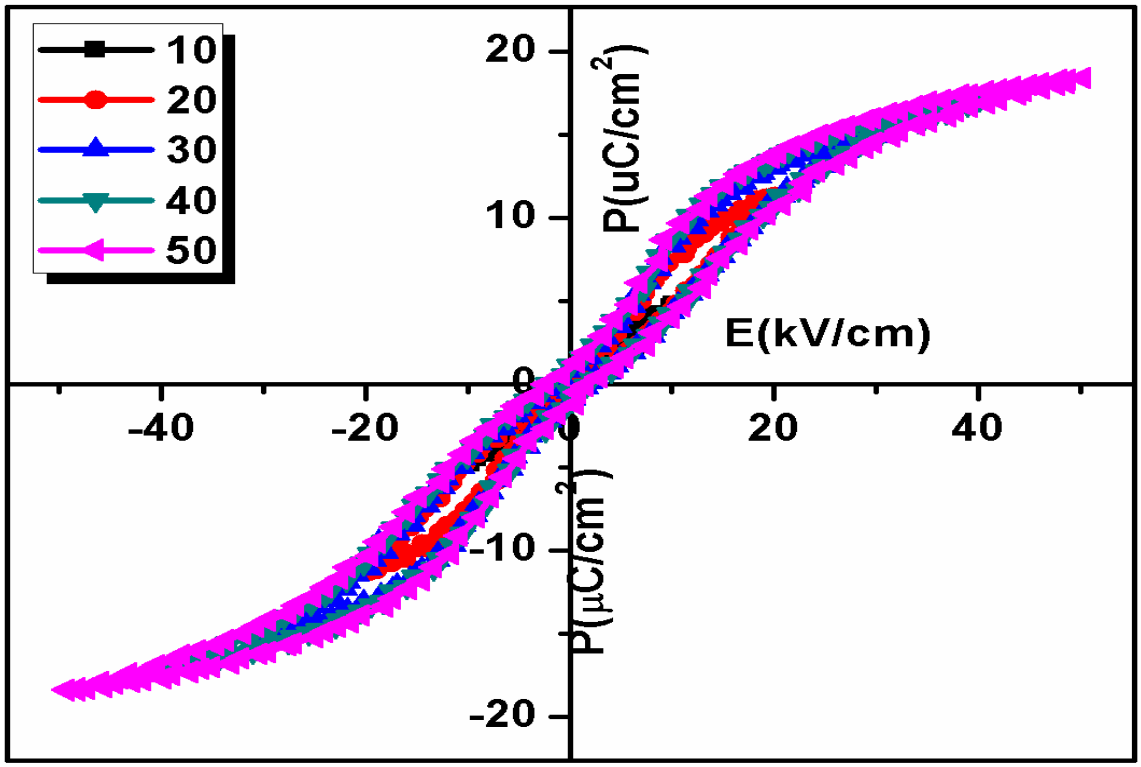

Fig. 11: P-E hysteresis loops of $BaTi_{0.97}(Zn,V,Ta)_{0.03}O_3$ ceramics.

Conclusion

$BaTi_{0.97}Zn_{0.01},V_{0.01}Ta_{0.01}O_3$ samples were fabricated using conventional using mixed oxide solid sintering route. The dopants did not induce any changes in symmetry and the sample crystallized into a tetragonal symmetry, confirmed by XRD and Raman spectroscopy. Electrical microstructure of the sample was studied using impedance spectroscopy which revealed that extrinsic conduction take place in the sample. A double hysteresis loop was observed for the sample and the energy storage density was 0.26 J/cm^3 under 50 kV/cm showing potential of these ceramics to be used for high density energy storage capacitors.

Acknowledgment

The authors acknowledge the financial support extended by Higher Education Commission (HEC) of Pakistan for the research fellowship at the Department of Materials Science and Engineering, University of Sheffield, United Kingdom.

References

1. X. Hao, J. Zhai, L. B. Kong, Z. Xu, A comprehensive review on the progress of lead zirconate-based antiferroelectric materials, *Prog. Mater. Sci.*, **63**, 1 (2014).
2. D. Makovec, Z. Samardžija, M. Drofenik, Solid solubility of holmium, yttrium, and dysprosium in $BaTiO_3$, *J. Am. Ceram. Soc.*, **87**, 1324 (2004).
3. R. Muhammad, Y. Iqbal, I. M. Reaney, $BaTiO_3$–$Bi(Mg_{2/3}Nb_{1/3})O_3$ Ceramics for High-Temperature Capacitor Applications, *J. Am. Ceram. Soc.*, **99**, 2089 (2016).
4. M. Uzair, Y. Iqbal, R. Muhammad, K. Hayat, I. M. Reaney, Effect of Li_3PO_4 addition on the sintering temperature, phase, microstructure, and electrical properties of $BaTiO_3$, *J. Mater. Sci.*, **50**, 1752 (2015).
5. M. Sebastian, H. Jantunen, Low loss dielectric materials for LTCC applications: a review, *Int. Mater. Rev.*, **53**, 57 (2008).
6. C. Sun, X. Wang, L. Li, Low sintering of X7R ceramics based on barium titanate with SiO_2–B_2O_3–Li_2O sintering additives in reducing atmosphere, *Ceram. Int.*, **38**, S49 (2012).
7. H. I. Hsiang, C. S. Hsi, C. C. Huang, S. L. Fu, Low temperature sintering and dielectric properties of $BaTiO_3$ with glass addition, *Mater. Chem. Phys.*, **113**, 658 (2009).
8. C. Sun, X. Wang, C. Ma, L. Li, Low-Temperature Sintering Barium Titanate-Based X8R Ceramics with Nd_2O_3 Dopant and ZnO–B_2O_3 Flux Agent, *J. Am. Ceram. Soc.*, **92**, 1613 (2009).
9. Y. Iqbal, A. Jamal, The effect of Ta_2O_5- and ZnO-doping on the Curie temperature of $BaTiO_3$, *J. Phys.: Conf. Ser.* (IOP Publishing, 2012).
10. B. H. Toby, EXPGUI, a graphical user interface for GSAS, *J. Appl. Crystallogr.*, **34**, 210 (2001).
11. X. Li, W. H. Shih, Size effects in barium titanate particles and clusters, *J. Am. Ceram. Soc.*, **80**, 2844 (1997).
12. Z. Lazarevic, N. Romcevic, M. Vijatovic, N. Paunovic, M. Rom·cevic, B. Stojanovic, Z. Doh·cevic-Mitrovic, Characterization of Barium Titanate Ceramic Powders by Raman Spectroscopy, *Proceedings of the Tenth Annual Conference of the Materials Research Society of Serbia*, (2008).
13. L. H. Robins, D. L. Kaiser, L. D. Rotter, P. K. Schenck, Investigation of the structure of barium titanate thin films by Raman spectroscopy, *J. Appl. Phys.*, **76**, 7487 (1994).
14. J. Pokorný, U. M. Pasha, L. Ben, O. P. Thakur, D. C. Sinclair, I. M. Reaney, Use of Raman spectroscopy to determine the site occupancy of dopants in $BaTiO_3$, *J. Appl. Phys.*, **109**, 114110 (2011).
15. A. Chauhan, S. Patel, R. Vaish, C. R. Bowen, Anti-Ferroelectric Ceramics for High Energy Density Capacitors, *Materials*, **8**, 8009 (2015).
16. P. S. Dobal, A. Dixit, R. S. Katiyar, Z. Yu, R. Guo, A. S. Bhalla, Phase transition behavior of $BaZr_xTi_{1-x}O_3$ ceramics, *J. Ram. Spec.*, **32**, 69 (2001).
17. R. Farhi, M. El Marssi, A. Simon, J. Ravez, A Raman and dielectric study of ferroelectric ceramics, *Eur. Phys. J. B*, **9**, 599 (1999).
18. R. Sagar, R. Raibagkar, Complex impedance and modulus studies of cerium doped barium zirconium titanate solid solution, *J. Alloys Compd.*, **549**, 206 (2013).
19. J. T. Irvine, D. C. Sinclair, A. R. West, Electroceramics: characterization by impedance spectroscopy, *Adv. Mater.*, **2**, 132 (1990).
20. G. Samara, Pressure and Temperature Dependences of the Dielectric Properties of the Perovskites $BaTiO_3$ and $SrTiO_3$, *Phys. Rev. B*, **151**, 378 (1966).
21. K. Uchino, E. Sadanaga, T. Hirose, Dependence of the crystal structure on particle size in barium titanate, *J. Am. Ceram. Soc.*, **72**, 1555 (1989).
22. M. Frey, D. Payne, Grain-size effect on structure and phase transformations for barium titanate, *Phys. Rev. B*, **54**, 3158 (1996).
23. N. Kumada, H. Ogiso, K. Shiroki, S. Wada, Y. Yonesaki, T. Takei, N. Kinomura, Rising Tc in

Bi and Cu Co-doped $BaTiO_3$, *Mater. Lett.*, **64**, 383 (2010).

24. H. Liu, B. Dkhil, A brief review on the model antiferroelectric $PbZrO_3$ perovskite-like material, *Zeitschrift für Kristallographie Crystalline Materials*, **226**, 163 (2011).
25. G. Yuan, Y. Yang, S. W. Or, Aging-induced double ferroelectric hysteresis loops in $BiFeO_3$ multiferroic ceramic, *Appl. Phys. Lett.*, **91**, 122907 (2007).
26. L. Zhang, X. Ren, In situ observation of reversible domain switching in aged Mn-doped $BaTiO_3$ single crystals, *Phys. Rev., B* **71**, 174108 (2005).
27. Z. Yu, Y. Liu, M. Shen, H. Qian, F. Li, Y. Lyu, Enhanced energy storage properties of $BiAlO_3$ modified $Bi_{0.5}Na_{0.5}TiO_3$–$Bi_{0.5}K_{0.5}TiO_3$ lead-free antiferroelectric ceramics, *Ceram. Int.*, **43**, 7653 (2017).